Available online at www.sciencedirect.com

jmr&t Journal of Materials Research and Technology

journal homepage: www.elsevier.com/locate/jmrt

Original Article

Effect of cerium (IV) on thin sulfuric acid anodizing of 2024-T3 alloy

R. del Olmo [a,*], *M. Mohedano* [a], *P. Visser* [b], *A. Rodriguez* [c], *E. Matykina* [a], *R. Arrabal* [a]

[a] *Departamento de Ingeniería Química y de Materiales, Facultad de Ciencias Químicas, Universidad Complutense de Madrid, 28040, Madrid, Spain*

[b] *AkzoNobel, Research & Development, Rijksstraatweg 31, Sassenheim, 2171, AJ, Netherlands*

[c] *Fundación Cidaut, Parque Tecnológico de Boecillo, 47151, Boecillo, Valladolid, Spain*

ARTICLE INFO

Article history:
Received 30 March 2021
Accepted 27 September 2021
Available online 7 October 2021

Keywords:
Anodizing
Aluminium
Cerium
Corrosion

ABSTRACT

Chromic acid anodizing (CAA) is still being used today for corrosion protection of fatigue-critical components in the aeronautic industry due to the lack of feasible alternatives. Ce-containing sulfuric acid anodizing (SAA) has been identified as a promising strategy for the development of alternatives to toxic CAA. This work explores thin sulfuric acid anodizing (TSAA) focusing on the following effects: (i) current density and voltage values; (ii) concentration of Ce(IV). Screening of the optimum combination in search of minimum thickness and the best corrosion resistance was performed using electrochemical impedance spectroscopy (EIS). Two Ce-containing anodic films were selected and further investigated in comparison with the inhibitor-free film in terms of morphology (FEG-SEM, TEM), composition (RBS), corrosion resistance (EIS, NSST), high-cycle fatigue and paint adhesion. The results indicate that the path to approach the CAA performance lies through thin (<1 μm) SAA-Ce films formed at low current density.

1. Introduction

Sulfuric acid anodizing (SAA) is widely used for corrosion protection of aluminium alloys such as 2024-T3 [1–3] which, due to its high strength-to-weight ratio, is extensively used for weight-sensitive applications in the aircraft industry. SAA can produce thick (~20 μm) and dense anodic oxide films (AOF) with relatively high corrosion resistance comprising an outer porous layer and a thin and compact barrier layer [4,5]. SAA operates under current and voltage that are typically within the ranges of 5–15 mA cm^{-2} and 15–40 V, respectively. These conditions result in anodic films with 7–15 nm pore size and a 1.15 nm V^{-1} barrier layer with a significant amount of incorporated sulfur [6,7].

SAA film thickness shows remarkable effects on corrosion, fatigue and paint adhesion. For the 2024-T3 alloy anodized at 15 mA cm^{-2}, Girginov et al. [5] reported values of impedance modulus (|Z| at 10^{-2} Hz) of $1 \cdot 10^4$ Ω cm^2 and $1 \cdot 10^5$ Ω cm [2], after immersion in 3.5 wt.% NaCl for 24 h, for ~5 μm- and ~17 μm-

* Corresponding author.
E-mail address: rubandom@ucm.es (R. del Olmo).
https://doi.org/10.1016/j.jmrt.2021.09.117

thick films, respectively. In similar studies, it was demonstrated that paint adhesion [8] and fatigue strength [9,10] were greatly reduced with increasing film thickness. This has led to the distinction between conventional SAA processes and thin sulfuric acid anodizing or TSAA [11–14]. The latter is designed to produce 3 μm-thick films in order to match the stringent fatigue requirements for aircraft structures. One of the main drawbacks of TSAA is its low corrosion resistance. One way to overcome this limitation is the incorporation of corrosion inhibitors during the anodizing process such as molybdate, permanganate and phosphate species [2,15–17].

Several authors have studied the effect of Ce-based compounds in SAA [18–22]. In general, better results in terms of corrosion resistance are reported for Ce(IV) species. For instance, Smith et al. [23] reported the effectiveness of cerium (IV) sulfate as an inhibitor in SAA: the unsealed 3-5 μm-thick films withstood up to 336 h in neutral salt spray test (NSST) till first pitting. Moutarlier et al. [24] also reported that $Ce(SO_4)_2$ increased the oxide growth rate. However, there is a lack of understanding of how Ce(IV) species influence anodizing efficiency and film morphology and composition. In the present study, these aspects together with the corrosion, fatigue and paint adhesion performances are investigated using two Ce(IV) concentrations, with $Ce(SO_4)_2$ salt as a source, in TSAA under constant current and constant voltage anodizing regimes. Note that $Ce(SO_4)_2$ has a higher solubility than $Ce_2(SO_4)_3$ in sulfuric acid which makes it a more convenient choice from a technological point of view [25].

2. Experimental procedures

2.1. Surface preparation

Rectangular 40 mm × 25 mm × 2 mm specimens of 2024-T3 (wt.%: 3.8–4.9 Cu, 1.2–1.8 Mg, 0.3–0.9 Mn, <0.5 Fe, <0.5 Si, <0.25 Zn, <0.15 Ti, <0.10 Cr and Al balance) were cleaned in 70 g L^{-1} BONDERITE C-AK 4215NC ($Na_2[B_4O_5(OH)_4]\cdot 8H_2O$, Fatty alcohol ethoxylate C10) solution for 10 min at 60 °C and etched in 85 g L^{-1} BONDERITE C-AK ALUM ETCH 2 AERO (NaOH, Na_3PO_4) for 2 min at 40 °C. Each procedure was followed by rinsing in deionized water. Finally, specimens were desmutted by immersion in BONDERITE C-IC SMUTGO NC AERO ($Fe_2(SO_4)_3$, HNO_3) for 5 min, rinsed in deionized water and dried with warm air. Supplementary Figure S1 shows the surface appearance of the 2024 alloy after the applied pretreatment, where it can be seen that most of the intermetallic particles have been removed. The working area was delimited to ~20 cm^2 using a commercial stopping-off resin (Lacquer 45, MacDermid plc.). The electrical connection was provided through a shielded copper wire.

2.2. Anodizing process

Anodic films were obtained using sulfuric acid (150 g L^{-1}) with different amounts of cerium (IV) sulfate (7.5 or 33 g L^{-1} $Ce(SO_4)_2$) at constant current density (1.5 or 15 mA cm^{-2}) or constant voltage (6 or 18 V), Table 1. The experimental system was equipped with a 1 L double-walled glass cell with a commercial fluid (HUBER SynOil, M10.120.08) running through a chiller (Huber minichiller Plus) to keep the electrolyte temperature at 298 K under continuous electrolyte agitation (300 rpm). The anodic films were formed using a DC power supply (SM400-AR-8 Systems electronic); a pure aluminium sheet (80 mm in diameter, 220 mm long and 0.5 mm thick) was used as a counter electrode. After anodizing, specimens were rinsed in deionized water, isopropanol and dried in warm air. Note that a CAA reference specimen provided by MTU Aero-Engines was also analyzed to compare its properties with the most promising anodic film.

Table 1 – Anodizing conditions of AA2024-T3 alloy.

Anodic film	Electrolyte (g L^{-1})		Conditions		
Designation	H_2SO_4	$Ce(SO_4)_2$	U (V)	j (mA cm^{-2})	Time (min)
S1	150	–	–	15	5
S2	150	–	–	15	15
S3	150	–	–	15	25
S4	150	–	–	1.5	5
S5	150	–	–	1.5	15
S6	150	–	–	1.5	25
S7	150	–	18[a]	–	25
S8	150	–	6[a]	–	113[b]
SC1.1	150	7.5	–	15	5
SC1.2	150	7.5	–	15	15
SC1.3	150	7.5	–	15	25
SC1.4	150	7.5	–	1.5	5
SC1.5	150	7.5	–	1.5	15
SC1.6	150	7.5	–	1.5	25
SC1.7	150	7.5	18[a]	–	25
SC1.8	150	7.5	6[a]	–	108[b]
SC2.1	150	33	–	15	5
SC2.2	150	33	–	15	15
SC2.3	150	33	–	15	25
SC2.4	150	33	–	1.5	5
SC2.5	150	33	–	1.5	15
SC2.6	150	33	–	1.5	25
SC2.7	150	33	18[a]	–	25
SC2.8	150	33	6[a]	–	140[b]

Note that constant voltage treatments included an initial ramp with a rate of 60 mV s^{-1}.
[a] An area of 150 cm^2 was used in order to get current values large enough for the acquisition system.
[b] Time adjusted to have a charge equal to that of 18 V treatment.

The ionic conductivity was measured using an EC Metro GLP 31 equipped with conductivity cell 5072 (C: 10 cm^{-1}). All the presented results provided the mean average value of all measurements.

2.3. Electrochemical impedance spectroscopy (EIS) screening

Anodized specimens with an exposed area of 1 cm^2 were tested in 3.5 wt.% NaCl naturally aerated solution at (22 ± 1)°C using a three-electrode cell connected to a GillAC computer-controlled potentiostat (ACM Instruments). Graphite rod and silver–silver chloride (Ag/AgCl, 3 M KCl) were used as counter and reference electrodes, respectively. A sinusoidal perturbation of 10 mV amplitude in the frequency range of 30

kHz–0.01 Hz was applied after 1 h of immersion. All measurements were repeated at least twice. Zview software was used to analyze and fit the EIS data. The goodness of fit was ensured through chi-squared values $\leq$ 0.01 (square of the standard deviation between the original data and the calculated spectrum). The obtained errors for the individual parameters of the equivalent electrical circuits were $\leq$5%. The anodic films with the highest total impedance at low frequencies ($|Z|_{10mHz}$) were selected for further studies.

2.4. *Surface characterization*

Anodic film morphologies were examined by transmission electron microscopy (JEM 2100, 200 kV) of ultramicrotomed sections prepared using a Leica Ultracut S instrument and a diamond knife (Microstar Technologies Inc., USA). Film thicknesses exceeding 2 μm were measured using an eddy-current meter (Fischer ISOSCOPE FMP10-FTA3.3H). Cited values are the average of ten measurements taken at arbitrary locations. TEM cross-sections were used for measuring thicknesses below 2 μm.

Compositions of anodic films were determined by Rutherford backscattering spectrometry (RBS) using an ion beam (He^+, 2 MeV) produced by a Van de Graff accelerator (CMAM, Autonomous University of Madrid). The incident ion beam with a diameter of 1 mm was normal to the specimen surface. 5–10 μC doze of scattered ions were detected by a mobile detector at 170°. Data were interpreted using SIMNRA software.

Contact angle measurements with deionized water were carried out on selected anodic films using an FTA 1000/FTA instrument. FTA32 software was used for the analysis of fifty photographs per drop at a frame rate of 0.5 s. Cited values are the average of measurements on two specimens using 3 drops on each.

Paint adhesion was evaluated on selected anodic films using three specimens per film following ISO 2409 standard. All paints were provided by AzkoNobel. They included two chromate-free solvent based epoxy-amine primers, of which Epoxy Primer 37,076 is a barrier primer and XP-420 is lithium-leaching primer that provides active corrosion protection [26]. Also, a Cr-bearing epoxy amine primer qualified for structural parts in the aircraft industry was used in combination with CAA film.

2.5. *Fatigue tests*

S–N curves were obtained at room temperature according to ASTM E466 at five strain levels, four repetitions per level, 15 Hz of frequency and 0.1 load ratio at room temperature. All measurements were performed using a servohydraulic test system (MTS 318HCF) with a load cell (MTS, 661.19F-12) and Termohigrometer (TESTO, 175-H2).

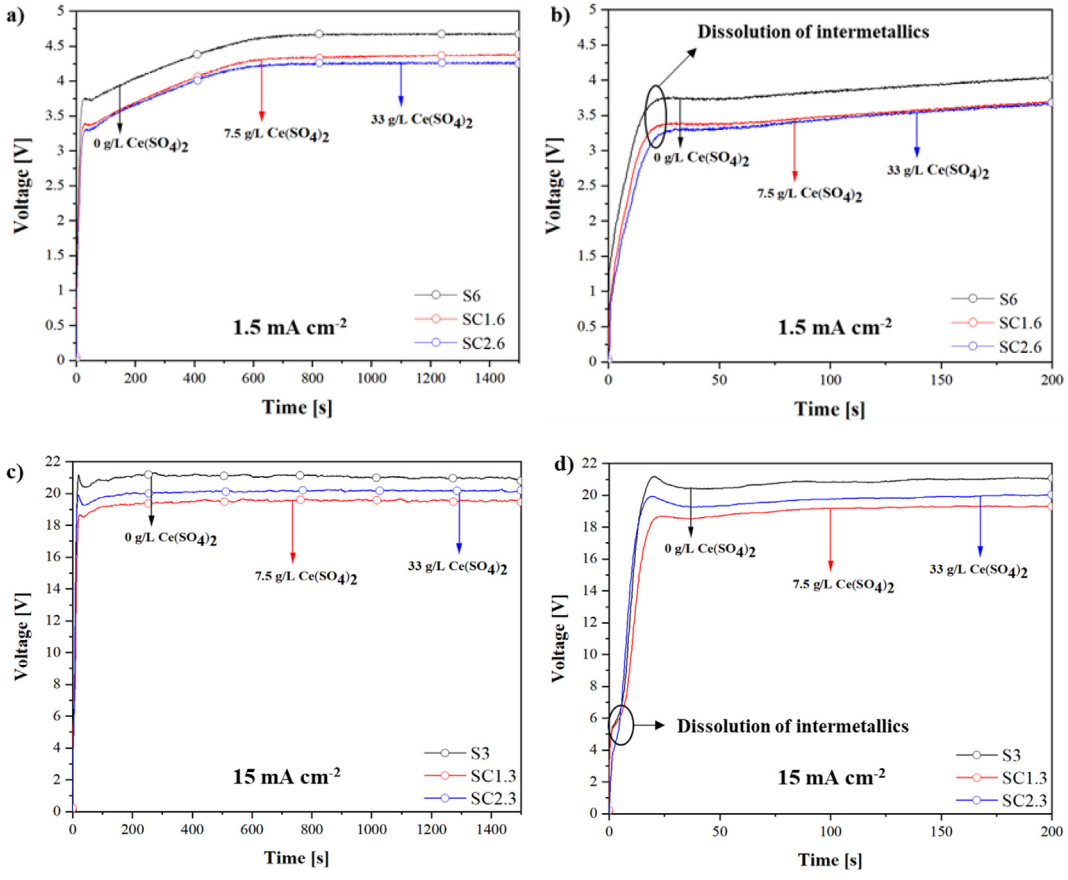

Fig. 1 – Voltage-time curves for anodizing with different amounts of $Ce(SO_4)_2$ at (a) 1.5 mA cm^{-2}, (b) 1.5 mA cm^{-2} at the beginning of the process and (c) 15 mA cm^{-2} and (d) 15 mA cm^{-2} at the beginning of the process.

2.6. Neutral salt spray test (NSST)

Triplicate 250 × 75 mm coupons were tested during 1000 h in a salt spray cabinet (CCI/CCM-MX, CCI) according to the ASTM B117 (5 wt. % NaCl, 6.5–7.2 pH and 35 °C). Specimens were inclined at 6° from the vertical. 50 mm × 50 mm cross was scribed in the center of coupons using a scratching tool (ISO 17872) with a 0.5 mm tungsten carbide tip. After the tests, the specimens were rinsed with deionized water at ~38 °C to remove solid salt deposits and dried with warm air. Rating numbers of scratched specimens were defined according to ASTM D 1654-92.

3. Results and discussion

3.1. Voltage- and current density-time responses

Figure 1 depicts the voltage-time responses under current-controlled mode for the 2024 alloy anodized at 1.5 (Fig. 1a,b) and 15 mA cm^{-2} (Fig. 1c,d). The voltage signal shows several changes that are related to phenomena such as thickening of the barrier layer, copper oxidation, oxygen evolution and dissolution of intermetallic particles [5]. As shown in Fig. 1, the voltage increases at a lower rate in the region between 3 and 6 V. This is more evident in the case of the low current regime (Fig. 1a,b) and is typically associated with the dissolution of intermetallic particles, such as S- (Al_2CuMg) and θ-phase (Al_2Cu) [3,27]. For longer anodizing times, the voltage signal reaches a steady state where the barrier layer maintains a constant thickness and the porous layer keeps developing. Final measured voltages are ~4–4.5 V and ~19.5–21 V for 1.5 mA cm^{-2} and 15 mA cm^{-2} curves, respectively. The larger voltage values for the higher current regimes are associated with the formation of a thicker barrier layer [28].

Regardless of the applied current density, the addition of $Ce(SO_4)_2$ decreases the final voltage by 0.5–1.5 V in comparison to the reference electrolyte (Fig. 1a,c). A similar effect was observed by Moutarlier et al. [24]. This could be to some extent due to the increased conductivity of the acidic solution. The measured electrolyte conductivities were: (339 ± 5) mS cm^{-1}, (639 ± 4) mS cm^{-1} and (660 ± 5) mS cm^{-1} for 0, 7.5 and 33 g L^{-1} $Ce(SO_4)_2$, respectively. These values, as opposed to those of Moutarlier (~240 μS cm^{-1} and 310 μS cm^{-1} without and with $Ce(SO_4)_2$, respectively), are consistent with the sulfuric acid concentration used in this work. Note that there is a non-linear increase in the conductivity of Ce-containing H_2SO_4, which may be related to the ionic interactions between Ce^{4+} and SO_4^{2-} and the formation of complexes [25].

However, if one considers these values and other parameters such as the cathode-to-anode distance (~4 cm), the size of the specimen (~20 cm^2) and the applied current, then the effect of electrolyte conductivity on measured voltage values should only be of the order of several millivolts. In fact, ~10 mV for 1.5 mA cm^{-2} and ~100 mV for 15 mA cm^{-2}. Therefore, the lower final voltages in the presence of $Ce(SO_4)_2$ are likely to be related to other factors, such as characteristics of the barrier layer (see Section 3.3).

The voltage-controlled treatments at 18 V (Fig. 2a) and 6 V (Fig. 2c) reveal several distinct features during the initial voltage ramp at 60 mV s^{-1}. Similarly to the contact current regime, the electrical response is affected by several phenomena such as thickening of the barrier layer, copper oxidation, oxygen evolution and dissolution of intermetallic particles.

The current increases from the commencement of anodizing until it reaches a plateau at ~1 mA cm^{-2} that lasts for ~15 s (this period corresponds to the interval between ~1.5 and 3 V). The initial current surge is related to the non-uniform thickening of the film, whereas the plateau is due to the constant field strength being maintained by uniform film growth [3]. Later, at ~95 s (i.e. ~5.7 V), there is a current peak which is again associated with the dissolution of secondary phases. Note that this peak is similar with and without Ce(IV) in the electrolyte, suggesting its little influence on the dissolution of intermetallic particles. After that, the current remains relatively constant at 2.3–2.8 mA cm^{-2} for the 6 V treatment, while a non-steady-state is observed in the case of the 18 V regime; the current density increases up to 17–19 mA cm^{-2} by the end of the treatment. This is due to heating of the electrolyte volume (by ~3 °C in the presence of a large size specimen) decreasing the overall resistance.

The presence of Ce(IV) species increases the final current density by approximately 0.5 and 2 mA cm^{-2} for 6 and 18 V curves, respectively. This is again in part due to the higher conductivity of the modified electrolyte and probably due to characteristics of the barrier layer (thickness and resistivity) in the presence of Ce(IV) species (see Section 3.3). Note that the concentrated electrolyte (33 g L^{-1}) yields lower current values than the dilute one (7.5 g L^{-1}) for the 18 V treatment.

3.2. Anodic films screening

The screening process to select TSAA anodic films with and without the studied Ce(IV) concentrations was according to (i) uniform surface appearance, (ii) the lowest possible thickness (≤3 μm) and (iii) the highest corrosion resistance.

As can be seen in Fig. 3, treatments developed at high current density (15 mA cm^{-2}) or high voltage (18 V) gave rise to the formation of thicker anodic films (≥2 μm) in comparison to low current density (1.5 mA cm^{-2}) and low voltage (6 V) treatments (<1 μm). This is consistent with the greater charge associated with longer treatment times and the higher current densities and voltages. Findings revealed that the thicknesses of Ce(IV)-containing electrolytes produced films of similar thickness to stand-alone TSAA films. This suggests that there is little or no incorporation of Ce species into the films.

Note that film thicknesses with values close to or below 1 μm should be taken with care as they are accompanied by a larger uncertainty associated with the limitations of the eddy current meter used for measuring film thickness.

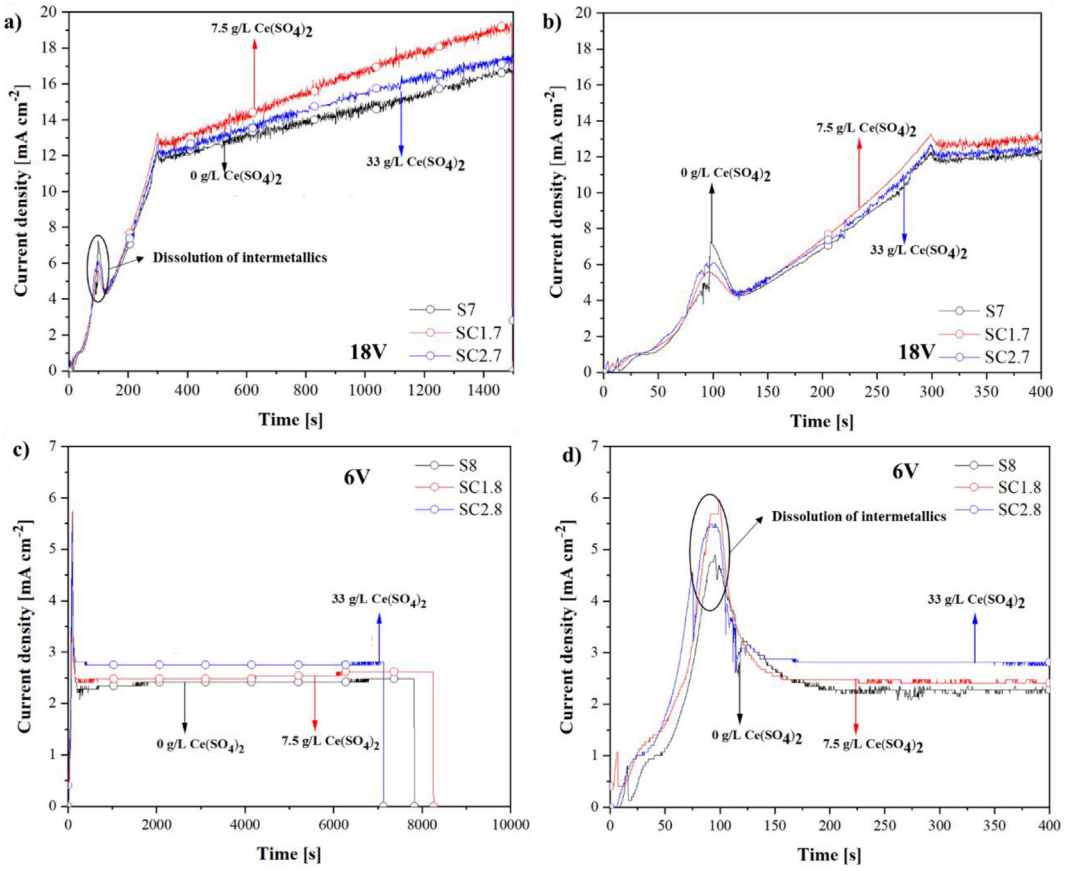

Fig. 2 – Current density-time curves for anodizing with different amounts of $Ce(SO_4)_2$ at (a) 18 V (b) 18 V at the beginning of the process, (c) 6 V and (d) 6 V at the beginning of the process. Plotted data in each case correspond to one specimen representative of five replicas.

Regarding the corrosion response, the anodic films developed under low current density show the best corrosion performance (Fig. 4). These results indicate an unusual non-linear dependence between film thickness and corrosion resistance [6]. This effect is more remarkable for the 1500 s treatments. The addition of Ce(IV) is in general positive, with SC1.6 (7.5 g L^{-1}, 1500s, 1.5 mA cm^{-2}) and SC2.6 (33 g L^{-1}, 1500s, 1.5 mA cm^{-2}) anodic films providing the best results. These specimens were further characterized and evaluated in terms of corrosion, paintability and fatigue life testing. The inhibitor-free anodic film S6 (0 g L^{-1}, 1500s, 1.5 mA cm^{-2}) was also analyzed for comparison.

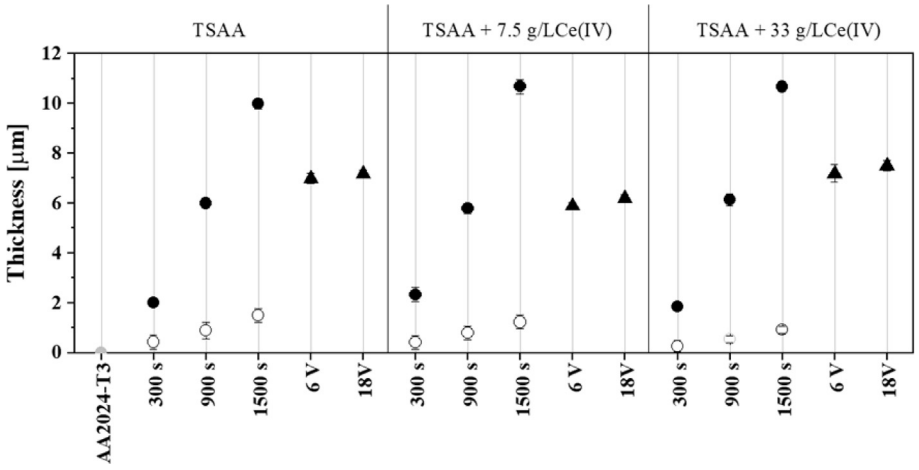

Fig. 3 – Scatter diagram of the thickness for Ce(IV)-TSAA films. Filled and empty circles indicate oxide films developed at 15 mA cm^{-2} and 1.5 mA cm^{-2}, respectively. Filled triangles indicate anodic films carried out under voltage-controlled mode.

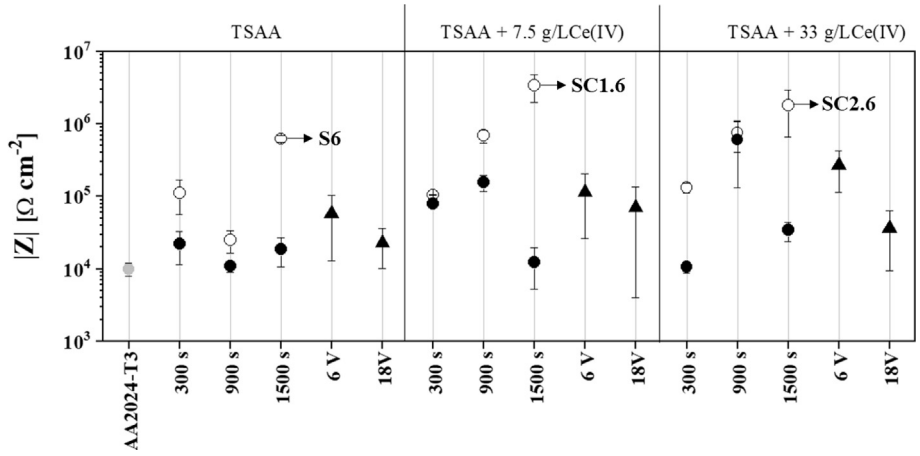

Fig. 4 – Scatter diagram of the impedance modulus at low frequencies values (10^{-2} Hz) for Ce(IV)-TSAA films. Filled and empty circles indicate oxide films developed at 15 mA cm^{-2} and 1.5 mA cm^{-2}, respectively. Filled triangles indicate anodic films carried out under voltage-controlled mode.

3.3. *Characterization of selected anodic films*

Figure 5 depicts the cross-sectional transmission electron micrographs of the selected anodic films; S6, SC1.6 and SC2.6. All the anodic films reveal a thin barrier layer and a porous layer with lateral porosity. This observation agrees with previous studies where the porous layer is strongly disorganized due to the presence of Cu-containing intermetallic particles

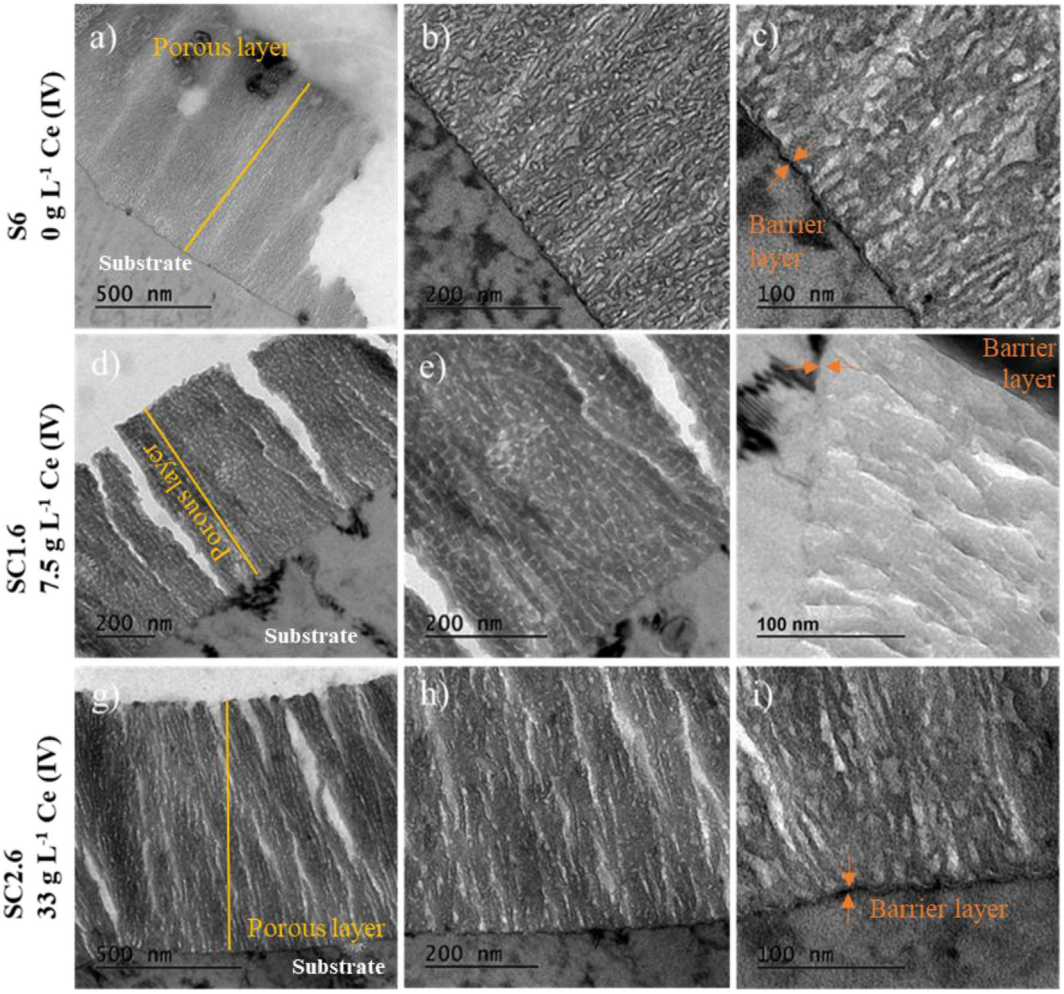

Fig. 5 – Transmission electron micrographs of anodic films: (a–c) S6, (d–f) SC1.6 and SC2.6 (g–i).

Table 2 – Film and barrier layer thickness values of the studied anodic films.

Anodic film/Property	S6	SC1.6	SC2.6
Film thickness (nm)	847 ± 16	689 ± 14	894 ± 8
Barrier layer thickness (nm)	4 ± 1	6 ± 1	5 ± 1
[a]Anodizing efficiency (%)	50	40	52

[a] Assuming the following values: ρAl_2O_3: 3.1 g cm^{-3}; porosity: 25%.

promoting oxygen evolution during the anodizing process [29].

Regarding the role of Ce on anodic film morphology, S6 showed a maze or chaotic pore alignment, whereas SC1.6 and SC2.6 films reveal more vertical and aligned pores. A similar change in pore morphology was observed by Li et al. [30] for the 1420 Al–Li alloy anodized in sulfuric acid, although the composition and the exact amount of Ce(IV) salt were not provided. Li et al. suggested that the change in pore morphology was associated with the surface adsorption of Ce-sulphate complexes which, in turn, affected the growth of the anodic film. It is also possible that the addition of Ce(IV) reduces oxygen evolution during anodizing, therefore decreasing the likelihood of lateral porosity. This statement is based on the lower voltage values recorded for the SC1.6 and SC2.6 specimens in comparison to S6.

Table 2 shows the measured values for oxide and barrier layer thickness. S6, SC1.6, and SC2.6 were all anodized at a constant current density of 1.5 mA cm^{-2} during 1500 s. Applying the Faraday's Law and assuming a 100% anodizing efficiency, the maximum achievable thickness is 1.7 μm. TSAA specimens show efficiencies in the range between ~40 and 50%, which are typical for sulfuric-based electrolytes [31,32].

According to Moutarlier, a ~20% increase in the growth rate was observed for 33 g L^{-1} Ce(IV) concentration in sulfuric acid electrolyte [24]. However, as already mentioned, this study does not provide direct evidence for this conclusion. Smith et al. reported a ~50% oxide film thickness decrease when incorporating 7.5 g L^{-1} of $Ce(SO_4)_2$ in a conventional sulfuric acid bath [23], but they did not specify the exact anodizing conditions and failed to provide visual evidence for this. In this study, eddy current measurements and TEM examination revealed a non-linear dependence between film thickness and Ce(IV) concentration in the electrolyte, with smaller thicknesses found for the SC1.6 specimen.

Measurements of the barrier layer thickness yielded values that correlated well with the final voltage values and the anodizing ratio of ~1 nm V^{-1} that is typically reported for sulfuric-based electrolytes [32]. The presence of Ce slightly increases the thickness of the barrier layer for SC1.6 (~6 ± 1 nm, 4.3 V) and SC2.6 (~5 ± 1 nm, 4.3 V) films in comparison to S6 reference specimen (~4 ± 1 nm, 4.5 V) (Table 2). Considering the lower final voltage values measured for these specimens, it is suggested in this work that Ce species facilitate charge transfer across the barrier layer, i.e. the anodizing ratio is above 1 nm V^{-1} in the Ce-containing solutions. Other studies where TEM characterization of Ce-SAA films has been performed do not provide high magnification micrographs of the barrier layer [33].

So far, this work has shown that the addition of $Ce(SO_4)_2$ modifies the voltage response, morphology and thickness of the anodic films developed in sulfuric acid under constant current conditions. The lower voltages are associated with the higher conductivity of the Ce-based electrolytes and possibly with the increased conductivity of the barrier layer in the presence of Ce species. The reduced lateral porosity of the anodic films developed in the presence of Ce(IV) is possibly linked to a lower amount of oxygen evolution during anodizing due to lower voltages [3,4]. With respect to anodic film thickness, the effect is less clear, although it seems that Ce addition tends to decrease the growth rate.

Many studies concerning the role of Ce species during anodizing fail to ascertain their role in film composition. One exception is the Ph.D. thesis by Banks [34] who using Rutherford backscattering spectroscopy reported very low or no detectable concentrations of cerium species (<0.003 at.%) in the 2024-T6 alloy anodized in sulfuric acid with $Ce(SO_4)_2$.

By applying the same characterization technique, the results shown in Fig. 6 were obtained for the S6, SC1.6 and SC2.6 specimens.

It is important to note that fitting was affected by the roughness of the films, consequently, the simulation of the spectra was performed as multi-layered systems.

The effects of the rough metal/film and film/air interfaces are reflected by the presence of sloping edges at ~400 and ~450 channels, which correspond to the presence of Cu and S through the oxide layers. S and Cu incorporation is a common feature of anodic films in 2024 alloy [35]. In all studied films, a step associated with the interface between the bulk alloy and the anodic film is revealed (~360 channel). Al manifested itself in the overall spectrum yield with two marked slopes at ~200 and ~360, which correspond to Al in the substrate and oxide, respectively.

Ce manifested as a small peak at the high energy end of the spectra (620–630 channel), which confirms its incorporation (~0.05 at.%) in the outer part (<6 nm-thick) of SC1.6 and SC2.6 anodic films (Fig. 6). The larger Ce incorporation in the SC2.6 film can be related to the higher Ce(IV) concentration in the electrolyte. It is also worth noting that a higher amount of S is detected in SC1.6 and SC2.6 specimens (~5.6 and 5.7 at.% *vs.* 2.8 at.% in S6) due to the higher sulfate (SO_4^{2-}) concentration in the electrolyte. The effect of Ce(IV) addition on Cu distribution in the oxide film can be considered negligible (Table 3).

It should be noted that, in principle, Ce^{4+} ions in sulfuric acid medium are positively charged and, therefore, are not supposed to be attracted by the electric field at the pore base and incorporated into the anodic oxide [36]. However, the RBS results indicate Ce incorporation in the outer region of the anodic film. This is possibly due to the formation of negatively charged sulfate complexes with Ce^{4+} which certainly can be attracted to the growing film. According to Paulenova et al. [25], the activity of free ceric cations (Ce^{4+}) is considerably

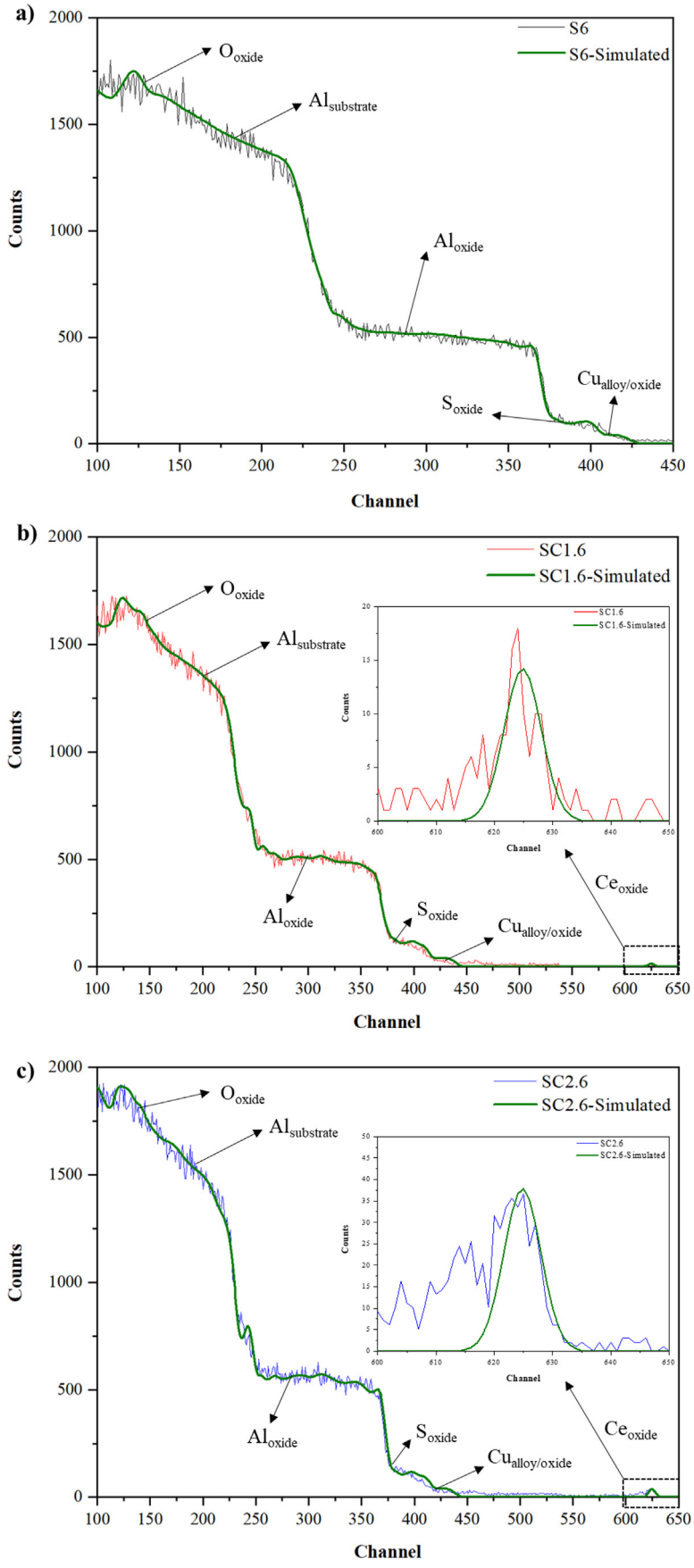

Fig. 6 – Experimental and simulated RBS spectra of (a) S6, (b) SC1.6 and (c) SC2.6 anodic films.

Table 3 – RBS results of S6, SC1.6 and SC2.6 anodic films.

Anodic film	Al_{oxide} (10^{20} at cm^{-2})	Cu_{oxide} (10^{20} at cm^{-2})	O_{oxide} (10^{20} at cm^{-2})	S_{oxide} (10^{20} at cm^{-2})	Ce_{oxide} (10^{20} at cm^{-2})
S6	0.803	0.015	1.670	0.073	–
SC1.6	0.675	0.017	1.533	0.131	0.001
SC2.6	0.765	0.018	1.602	0.145	0.002

lower than its formal concentration, because practically all the Ce^{4+} in sulfuric acid medium is complexed and present as negatively charged complex, *i.e.* $Ce(SO_4)_3^{2-}$ [25]. On the other hand, as stated in the work by Paulenova, Ce^{3+} tends to form a positively charged complex $[Ce(SO_4)]^+$, that would not be attracted to the anode. This supports the choice of $Ce(SO_4)_2$ over $Ce_2(SO_4)_3$ as an additive.

These results support the idea that $Ce(SO_4)_2$ additive favours the delivery of additional SO_4^{2-} into the growing anodic film through the formation of $Ce(SO_4)_3^{2-}$ complex as a transporter. Once incorporated into the film, it is expected that the complex dissociates, resulting in the transport of SO_4^{2-} towards the metal/oxide interface and Ce^{4+} towards the oxide/electrolyte interface. The latter would explain the preferential location of Ce in the outer region of the film. The enhanced incorporation of S in the film could also contribute to the reduced lateral porosity of the films through the generation of compressive stresses [37].

Considering the RBS results and the previous observations in regards to reduced voltage values and the thicker barrier layer in the presence of Ce(IV) (see Fig. 1 and Table 2), it stands to reason that the enhanced charge transfer resistance of the barrier layer is related to compositional changes in this layer. In a recent study by Elabar et al. [37], it was also shown that the presence of additional SO_4^{2-} ions in the electrolyte increased the ionic transport (i.e. mobility of defects) across the film during anodizing. This effect was ascribed to changes in the space charge and structure of the film. Additionally, the presence in the outer regions of the film of Ce^{4+} ions, with higher charge and ionic radius than Al^{3+}, may facilitate the creation of point defects in the oxide structure due to larger electrostrictive strains [6].

3.4. *Corrosion behaviour*

Figure 7 shows the Bode and Nyquist diagrams with the fitted results for S6, SC1.6, and SC2.6 selected anodic films after immersion in 3.5 wt. % NaCl solution at 1 h and 28 days. Figure S2 displays Bode diagrams (|Z| vs f) at intermediate immersion times for selected specimens.

For 1 h of immersion, there are two relaxation processes related to the responses of the outer porous and inner barrier layers of the coatings at high and low frequencies, respectively. The protective behaviour of SC1.6 and SC2.6 films is evident in the Bode plots since a marked slope is observed in the entire frequency range, denoting the low mobility of the corrosive ions through the layer in comparison to S6 anodic film [11].

After 28 days of immersion, all the specimens show a decrease of the low-frequency impedance modulus (10^{-2} Hz) associated with partial loss of the barrier effect of the anodic film [13,16,38,39]. The penetration of Cl^- anions towards the substrate is also revealed by the degradation of the outer porous layer since the time constant at high frequencies almost disappears. In any case, SC1.6 and SC2.6 show better corrosion resistance than the S6 film.

Figure 8 provides the schematic illustration of the corresponding equivalent circuit to interpret the EIS results for studied specimens after 1 h (Table 4) and 28 days (Table 5) of immersion. The use of constant phase elements (CPE) instead of capacitors is mainly due to the non-ideal nature of the developed anodic films (e.g. roughness and defects).

In both equivalent circuits, R_{sol} (150–300 Ω cm^2) represents the solution resistance, CPE_{por}/R_{por} are associated with the porous layer, and CPE_b/R_b correspond to the barrier layer [11]. After 28 days of immersion, the equivalent circuit in Fig. 8b was used. This includes the CPE_{pw} or the capacitive response of the pore walls due to their gradual degradation with time [40].

For 1 h of immersion time (Table 4), the beneficial effect of Ce(IV) addition into sulfuric acid electrolyte is evident since the R_b value of the reference anodic film (S6) was one order of magnitude lower than those of SC1.6 and SC2.6. This protective barrier effect was likewise confirmed by the near-capacitive behaviour of the SC1.6 and SC2.6 films (*n* value closer to 1) in comparison with S6.

After 28 days of immersion, there is a decrease in the barrier-related resistance values and the corresponding increase of CPE values (Table 5). This indicates that the electrolyte can penetrate through the anodic films leading to their gradual degradation [2,40].

The superior response of Ce-containing films may be explained by several factors. The higher R_b values are consistent with the thicker barrier layer evidenced by the TEM examination. Ce-containing films show reduced lateral porosity (i.e. a higher structural stability of the porous layer) which has been attributed in this study to reduced oxygen evolution and compressive stresses generated by enhanced S incorporation. Further, cationic dopants in the alumina film, in our case Ce(IV), may reduce the isoelectric point of the oxide [41]. In case the isolelectric point is below the pH of neutral solutions, the oxide surface would be negatively charged (i.e. hydroxylated) and would repel Cl-ions that tend to destroy the passivity. On a negatively charged surface, the heat of adsorption of Cl^- (one of the main contributors to the anodic current in the pit initiation process [41]) would be lower and so would be the anodic current. As a result, greater polarization would be needed to achieve the critical pitting current and potential. Cationic dopants with greater valence than the matrix cations (Ce^{4+} vs. Al^{3+}) also decrease the number of oxygen vacancies in order to maintain charge neutrality: the excessive positive charge is compensated with

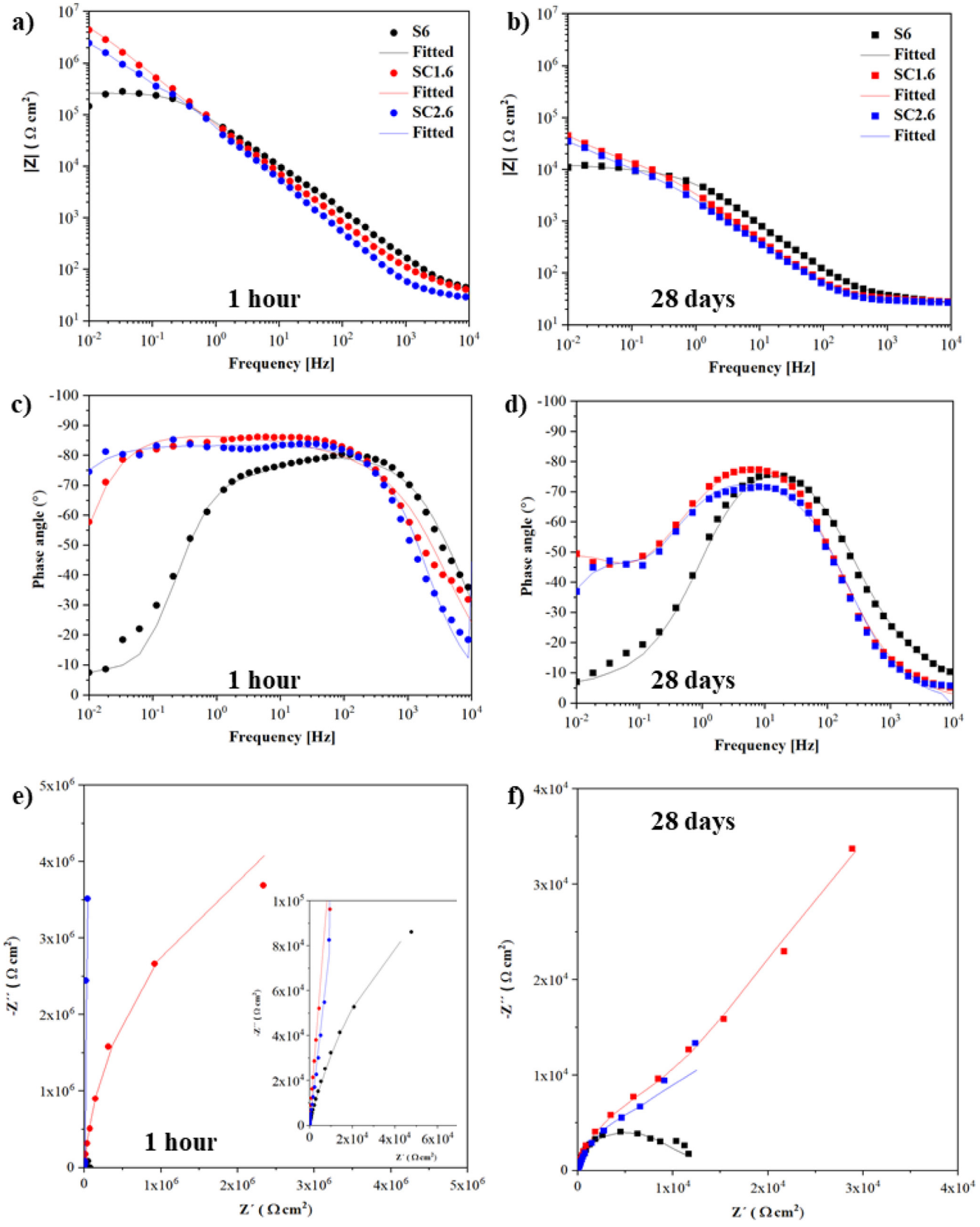

Fig. 7 – (a–d) Bode and (e,f) Nyquist plots of all selected specimens after 1 h and 28 days of immersion in 3.5 wt. % NaCl solution.

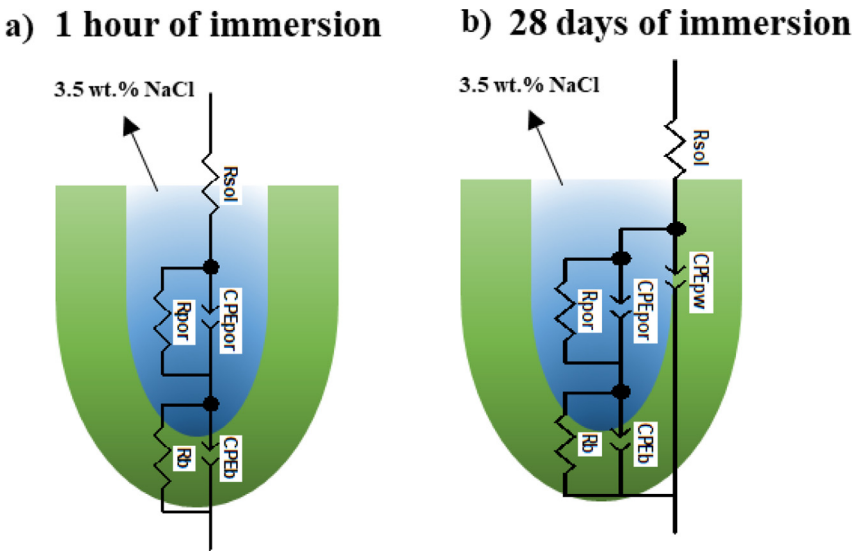

Fig. 8 – Equivalent circuits used to fit the experimental EIS data: (a) 1 h and (b) 28 days.

free electrons brought in when a vacancy is occupied with an oxygen anion. This makes it more difficult for Cl^- anions to migrate through the anion vacancies in the oxide film, and the passivity is easier to maintain. The presence of Ce^{4+} in the outer part of the oxide film may also induce precipitation of Ce(IV) oxides/hydroxides when the pH is higher than 3 [42,43]. This Ce(IV) may come from Ce incorporated in the alumina film and from the electrolyte remnants within the pores.

3.5. *Paint adhesion evaluation*

Contact angle and paint adhesion measurements are presented in Fig. 9. The CAA reference sample was also included for comparison.

Water contact angle is a useful tool that informs about the surface wettability, e.g. a lower contact angle typically corresponds to a higher paintability. Present findings reveal that all studied anodic films are hydrophilic (contact angles <90°) [44]. The literature studies on paint adhesion to anodic films are limited but, in general, good results are achieved largely due to the typical porous morphology of anodic films [45,46].

The paintability testing was performed according to ISO 2409 standard on selected anodic films using a commercial paint (Epoxy Primer 37,076) provided by *AkzoNobel*.

The observed differences in paint adhesion of SC1.6 and SC2.6 (rating 0) in comparison to S6 anodic film (rating 1) may be related to (i) to the presence of Ce(IV) in the outer region of the anodic films, as observed by RBS, with the studied paint and (ii) pore alignment that favours the paint penetration throughout the film as seen in TEM micrographs (Fig. 5).

3.6. *NSST evaluation*

An additional corrosion test based on the ASTM D1654-92 standard was performed for SC1.6 film since it showed the best overall corrosion resistance-to-thickness ratio among all the selected specimens (Fig. 10). The CAA reference sample was also included for comparison.

The test consists in exposure of 250 mm × 75 mm × 2 mm painted and scratched coupons in a salt fog environment (5 wt. % NaCl at 6.5–7.2 pH range and 35 °C) for 1000 h. Note that the "chromated" paint was used as a reference to

Table 4 – Fitted electrical parameters of EIS spectra after 1 h of immersion in 3.5 wt.% NaCl.

Anodic film	CPE_{por} ($F\ s^{(n-1)}\cdot cm^{-2}$)	n	R_{por} ($\Omega\ cm^2$)	CPE_b ($F\ s^{(n-1)}\cdot cm^{-2}$)	n	R_b ($\Omega\ cm^2$)
S6	$3.9\cdot10^{-6}$	0.98	$4.2\cdot10^{4}$	$2.6\cdot10^{-6}$	0.88	$2.5\cdot10^{5}$
SC1.6	$6.5\cdot10^{-5}$	0.89	$1.0\cdot10^{5}$	$2.7\cdot10^{-6}$	0.98	$8.9\cdot10^{6}$
SC2.6	$2.4\cdot10^{-6}$	0.92	$1.8\cdot10^{5}$	$5.7\cdot10^{-5}$	0.98	$3.0\cdot10^{6}$

Table 5 – Fitted electrical parameters of EIS spectra after 28 days of immersion in 3.5 wt.% NaCl.

Anodic film	CPE_{pw} ($F\ s^{(n-1)}\cdot cm^{-2}$)	n	CPE_{por} ($F\ s^{(n-1)}\cdot cm^{-2}$)	n	R_{por} ($\Omega\ cm^2$)	CPE_b ($F\ s^{(n-1)}\cdot cm^{-2}$)	n	R_b ($\Omega\ cm^2$)
S6	$4.5\cdot10^{-5}$	0.81	$5.9\cdot10^{-3}$	0.85	$7.9\cdot10^{2}$	$2.1\cdot10^{-5}$	0.96	$1.7\cdot10^{4}$
SC1.6	$6.0\cdot10^{-5}$	0.77	$5.9\cdot10^{-6}$	0.98	$1.8\cdot10^{3}$	$1.3\cdot10^{-4}$	0.71	$2.6\cdot10^{5}$
SC2.6	$3.9\cdot10^{-5}$	0.75	$5.4\cdot10^{-5}$	0.97	$7.8\cdot10^{3}$	$1.8\cdot10^{-4}$	0.78	$5.9\cdot10^{4}$

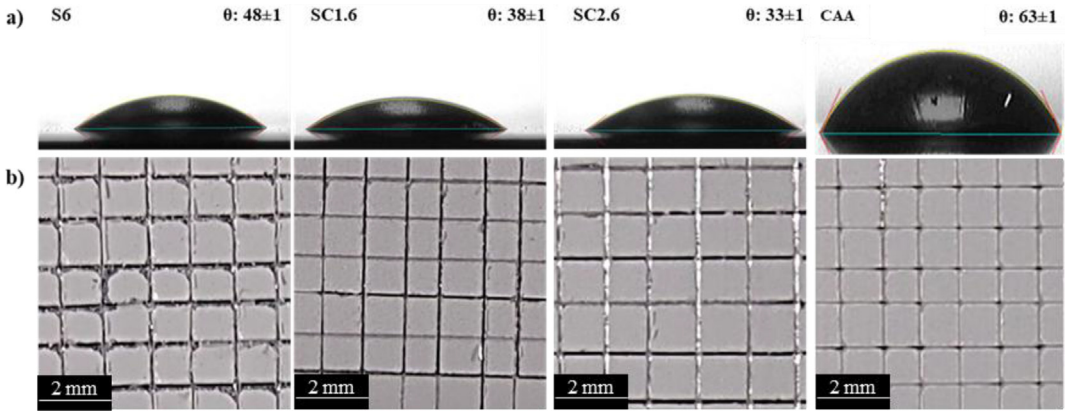

Fig. 9 – (a) Water contact angle with as-received anodic films and (b) surface appearance of painted anodic films after the adhesion test. S6-rating 1, SC1.6-rating 0, SC2.6-rating 0 and CAA-rating 0.

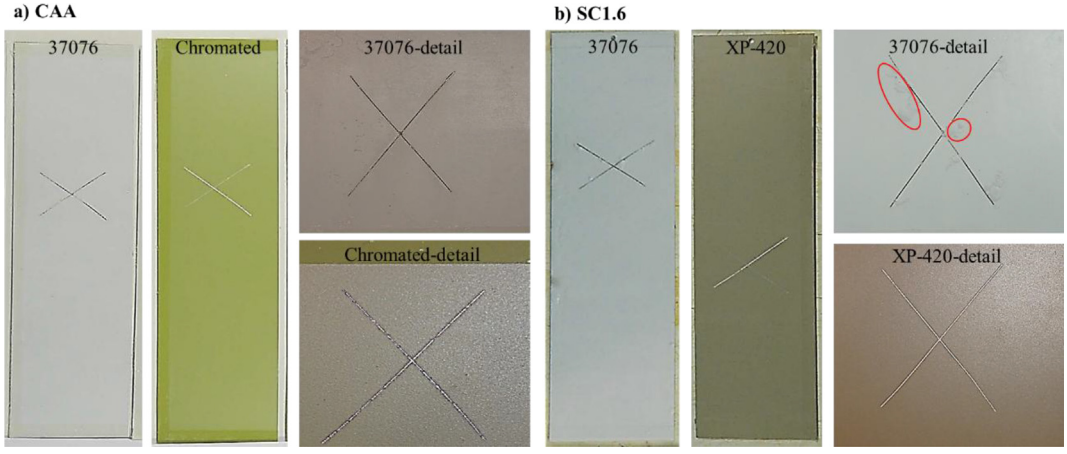

Fig. 10 – Macrographs of (a) CAA and (b) SC1.6 painted specimens after 1000 h of NSST as per ASTM D1654-92. Red circles indicate the presence and location of blisters.

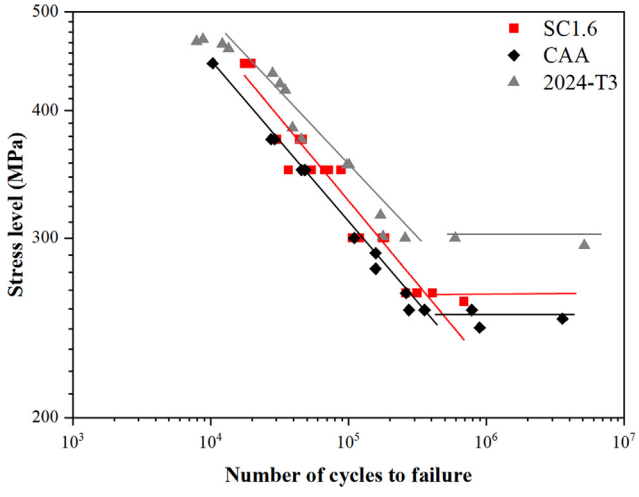

Fig. 11 – Fatigue life of CAA reference sample, SC1.6 anodic film and 2024 alloy.

reproduce a typical full system protection applied by the aircraft industry to CAA films.

As shown in Fig. 10, SC1.6 anodic film with the inhibitor-free paint (37,076) revealed ~3 ± 0.5 mm and ~5 ± 0.4 mm blisters after 1000 h, respectively. These results are worse than the CAA ones with the same paint, which did not show signs of corrosion. Better results were obtained for these specimens when the active protection-bearing paint (XP-420) was used since no blisters were observed and the performance was comparable to that of CAA. Compared to other studies [45,46], which obtained a similar corrosion performance with thicker anodic films, present findings are highly relevant since a comparable corrosion resistance to CAA can be reached with thinner anodic films and produced in shorter times.

3.7. *Fatigue evaluation*

Fatigue life curve for the SC1.6 specimen is presented in Fig. 11. CAA reference sample and the 2024-T3 alloy are also evaluated. The highest endurance limit, measured after 10^7 cycles, was 300 MPa for the bare 2024 alloy. Values of 265 and

256 MPa were measured for SC1.6 and CAA, respectively. It is known that the anodizing process reduces the fatigue strength by the formation of pit-like cavities at the film–substrate interface during anodizing in the active Cu-intermetallic particles. This produces local stress concentration points, leading to crack propagation under loading [47,48].

A well-known factor in the fatigue life of anodic layers is the coating thickness since the passage of the fatigue cracks from the coating to the substrate is favoured at higher thickness values [48,49]. For instance, Rateick [48] et al., report maximum stress values at 10^6 cycles of 210 and 225 MPa for SAA (5 μm) and CAA (1.6 μm) anodic films.

The obtained results suggested that anodic film thickness was not the main factor for the fatigue life increase since SC1.6 thickness is similar to the CAA-reference sample (0.7 μm). This is also in accordance with other studies where other factors such as the pits formed during the anodizing and the ductility/brittleness of the anodized layer can act as stress raisers during fatigue loading. This can significantly affect the fatigue life, thus spreading cracks into the underlying substrate material [50–52]. From the fatigue endurance point of view, the developed anodic films performed favourably compared with CAA film.

4. Conclusions

- Ce(IV)-containing anodic films formed at 1.5 mA cm^{-2} for 1500 s with <1 μm thickness and ~1–6 × 10^6 Ω cm^2 impedance modulus in 3.5% NaCl showed the best short-term corrosion performance among studied TSAA-based films, which is mainly due to the thicker barrier layer and reduced lateral porosity of the films in comparison to the stand-alone TSAA film.
- Ce is incorporated in the outer region of the film (<6 nm, 0.01–0.02·10^{20} at cm^{-2}). The enhanced incorporation of S in Ce-containing films likely increased the charge transfer and lowered the voltage during film growth. Reduced lateral porosity of the film is attributed to reduced oxygen evolution and generation of compressive stresses.
- The presence of Ce in the outer region of the films and enhanced pore alignment lead to an improvement in the paint adhesion. TSAA with 7.5 g L^{-1} of $Ce(SO_4)_2$ reveals the best results in terms of corrosion resistance-thickness, paint adhesion, fatigue resistance and corrosion behaviour after 1000 h of exposure time in NSST.

In summary, present findings reveal that <1 μm-thick Ce-containing TSAA formed at 1.5 mA cm^{-2} on 2024-T3 in painted conditions can be recommended for exploitation on an industrial level to replace CAA in painted- and corrosion-sensitive applications. Further research of these anodic films on industrial testing purposes is needed to reveal their full potential for key fatigue-sensitive applications.

Data statement

The raw/process data required to reproduce these findings cannot be shared at this time as the data also forms part of an ongoing study.

Declaration of Competing Interest

The authors declare that they have no known competing financial interests or personal relationships that could have appeared to influence the work reported in this paper.

Acknowledgements

The authors gratefully acknowledge the support of the ALMAGIC project (H2020 Clean Sky 2, Grant agreement Nº 755515), RTI2018-096391-B-C33 (MCIU/AEI/FEDER, UE) and ADITIMAT-CM (S2018/NMT-4411, Regional Government of Madrid and EU Structural and Social Funds). M. Mohedano is grateful for the support of RYC-201721843.

Appendix A. Supplementary data

Supplementary data to this article can be found online at https://doi.org/10.1016/j.jmrt.2021.09.117.

REFERENCES

[1] Elaish R, Curioni M, Gowers K, Kasuga A, Habazaki H, Hashimoto T, et al. Effect of fluorozirconic acid on anodizing of aluminium and AA 2024-T3 alloy in sulphuric and tartaric-sulphuric acids. Surf Coating Technol 2018;342:233.
[2] Moutarlier V, Gigandet MP, Normand B, Pagetti J. EIS characterisation of anodic films formed on 2024 aluminium alloy, in sulphuric acid containing molybdate or permanganate species. Corrosion Sci 2005;47(4):937.
[3] Curioni M, Saenz de Miera M, Skeldon P, Thompson G, Ferguson J. Macroscopic and local filming behavior of AA2024 T3 aluminum alloy during anodizing in sulfuric acid electrolyte. J Electrochem Soc 2008;155:C387.
[4] Torrescano-Alvarez JM, Curioni M, Skeldon P. Effects of oxygen evolution on the voltage and film morphology during galvanostatic anodizing of AA 2024-T3 aluminium alloy in sulphuric acid at −2 and 24 °C. Electrochim Acta 2018;275:172.
[5] Girginov C, Kozhukharov S, Milanes M, Machkova M. Impact of the anodizing duration on the surface morphology and performance of A2024-T3 in a model corrosive medium. Mater Chem Phys 2017;198:137.
[6] Runge JM. Anodic aluminum oxide growth and structure. In: The metallurgy of anodizing aluminum. Cham: Springer; 2018.
[7] Sulka G. Highly ordered anodic porous alumina formation by self-organized anodizing. In: Eftekhari A, editor. Nanostructured materials in electrochemistry. Wiley-VCH Verlag; 2008. p. 1–116.
[8] Abrahami ST, Hauffman T, de Kok JMM, Mol JMC, Terryn H. Effect of anodic aluminum oxide chemistry on adhesive bonding of epoxy. J Phys Chem C 2016;120(35):19670.
[9] Fares C, Hemmouche L, Belouchrani MA, Amrouche A, Chicot D, Puchi-Cabrera ES. Coupled effects of substrate microstructure and sulphuric acid anodizing on fatigue life of a 2017A aluminum alloy. Mater Des 2015;86:723.
[10] Priet B, Odemer G, Blanc C, Giffard K, Arurault L. Effect of new sealing treatments on corrosion fatigue lifetime of anodized 2024 aluminium alloy. Surf Coating Technol 2016;307:206.

[11] Balaraju JN, Srinivasan A, Yoganandan G, William Grips VK, Rajam KS. Effect of Mn/Mo incorporated oxide layer on the corrosion behavior of AA 2024 alloy. Corrosion Sci 2011;53(12):4084.
[12] Lee SJ, Kim SJ. Evaluation of durability depending on two step anodizing process time using sulfuric acid electrolyte. J Nanosci Nanotechnol 2019 Apr 1;19(4):2291–4.
[13] Ding Z, Smith BA, Hebert RR, Zhang W, Jaworowski MR. Morphology perspective on chromic acid anodizing replacement by thin film sulfuric acid anodizing. Surf Coating Technol 2018;350:31.
[14] Ding Z. Mechanistic study of thin film sulfuric acid anodizing rate difference between Al2024 T3 and Al6061 T6. Surf Coating Technol 2019;357:280.
[15] Mohammadi M, Yazdani A, Bahrololoom ME, Alfantazi A. Corrosion behavior of 2024 aluminum alloy anodized in presence of permanganate and phosphate ions. J Coating Technol Res 2013;10(2):219.
[16] Mohammadi M, Yazdani A, Mohammadi F, Alfantazi A. Corrosion behavior of 2024 aluminum alloy anodized in sulfuric acid containing inorganic inhibitor. TMS Light Metals; 2013. p. 509–13.
[17] Moutarlier V, Gigandet MP, Pagetti J, Ricq L. Molybdate/sulfuric acid anodising of 2024-aluminium alloy: influence of inhibitor concentration on film growth and on corrosion resistance. Surf Coating Technol 2003;173(1):87.
[18] Zhao JM, Liu HX, Chen SL, Zhao XH. EIS evolution of anodised aluminium by cerium salt sealing in NaCl solution with exposure time. Corrosion Eng Sci Technol 2013;48(1):44.
[19] F. Mansfeld, C. Chen, C. Breslin and D. Hull: Sealing of anodised aluminium alloys with rare earth metal salt solutions, J Electrochem Soc, 145 (8). pp. 2792-2798.
[20] Curioni M, Zuleta AA, Correa E, Pan X, Baron-Wiechec A, Skeldon P, et al. Formation of protective anodic oxides on aluminium by low voltage anodising in sulphuric acid with cerium nitrate and tartaric acid additions. Transac IMF 2012;90(6):290.
[21] Q. Zheng Li, Y. Zuo, J. Mao Zhao, Y. Ming Tang, X. Hui Zhao and J. Ping Xiong: Corrosion behaviors of Ce- and Nd-modified anodic films on aluminum, Anti-corrosion Methods & Mater, 57(5), 238-243.
[22] Li D, Peng Deng Y, Lan Guo B, Qiang Li G. Investigation of cerium salt/sulfuric acid anodizing technology for 1420 aluminum alloy. Mater Sci Forum 2000;331–337(3).
[23] Smith C.J.E. BKR, Evans VM, Garrett SA, Smith KS. Research into chromate- free treatments for protection of aluminium alloys. AGARD Report; 1997.
[24] Moutarlier V, Gigandet MP, Pagetti J, Normand B. An electrochemical approach to the anodic oxidation of Al 2024 alloy in sulfuric acid containing inhibitors. Surf Coating Technol 2002;161(2):267.
[25] Paulenova A, Creager S, Navratil JD, Wei Y. Redox potentials and kinetics of the Ce^{3+}/Ce^{4+} redox reaction and solubility of cerium sulfates in sulfuric acid solutions. J Power Sources 2002;109:431.
[26] Visser P, Liu Y, Terryn H, Mol JMC. Lithium salts as leachable corrosion inhibitors and potential replacement for hexavalent chromium in organic coatings for the protection of aluminum alloys. J Coating Technol Res 2016;13(4):557.
[27] Saenz de Miera M, Curioni M, Skeldon P, Thompson G. Preferential anodic oxidation of second-phase constituents during anodising of AA2024-T3 and AA7075-T6 alloys. Surf Interface Anal 2010;42:241.
[28] Ecco LG, Fedel M, Deflorian F, Becker J, Iversen BB, Mamakhel A. Waterborne acrylic paint system based on nanoceria for corrosion protection of steel. Prog Org Coating 2016;96:19.
[29] Arenas-Vara M, Skeldon P, García-Vergara S. Effect of copper-enriched layers on localized corrosion of aluminium-copper alloys. Rev Fac Ing 2018;27:7.
[30] Li D, Peng Deng Y, Lan Guo B, Qiang Li G. Investigation of cerium salt/sulfuric acid anodizing technology for 1420 aluminum alloy. Mater Sci Forum 2000;1695.
[31] Iglesias-Rubianes L, Garcia-Vergara S, Skeldon P, Thompson G, Ferguson J, Beneke M. Cyclic oxidation processes during anodizing of Al–Cu alloys. Electrochim Acta 2007;52:7148.
[32] Mingo B, Němcová A, Hamad D, Arrabal R, Matykina E, Curioni M, et al. Efficiency of anodising of Al–Cu alloy in sulphuric acid at low potentials. Transac IMF 2015;93:18.
[33] Curioni M, Skeldon P, Thompson GE. 5 - anodized anti-corrosion coatings for aluminium using rare earth metals. In: Forsyth M, Hinton B, editors. Rare earth-based corrosion inhibitors. Woodhead Publishing, City; 2014. p. 143.
[34] Banks T. Corrosion control of aluminium alloys through novel anodizing processes (PhD Thesis). University of Manchester; 2006.
[35] Torrescano-Alvarez JM, Curioni M, Habazaki H, Hashimoto T, Skeldon P, Zhou X. Incorporation of alloying elements into porous anodic films on aluminium alloys: the role of cell diameter. Electrochim Acta 2019;296:783.
[36] Wang H, Wang HW. Analysis on porous aluminum anodic oxide film formed in Re–OA–H_3PO_4 solution. Mater Chem Phys 2006;97(2):213.
[37] Elabar D, La Monica GR, Santamaria M, Di Quarto F, Skeldon P, Thompson GE. Anodizing of aluminium and AA 2024-T3 alloy in chromic acid: effects of sulphate on film growth. Surf Coating Technol 2017;309:480.
[38] Khan MF, Kumar AM, Ul-Hamid A, Al-Hems LM. Achieving non-adsorptive anodized film on Al-2024 alloy: surface and electrochemical corrosion investigation. Surf Interf 2019;15:78.
[39] Moutarlier V, Gigandet MP, Ricq L, Pagetti J. Electrochemical characterisation of anodic oxidation films formed in presence of corrosion inhibitors. Appl Surf Sci 2001;183(1–2):1.
[40] Capelossi VR, Poelman M, Recloux I, Hernandez RPB, de Melo HG, Olivier MG. Corrosion protection of clad 2024 aluminum alloy anodized in tartaric-sulfuric acid bath and protected with hybrid sol–gel coating. Electrochim Acta 2014;124:69.
[41] McCafferty E. A surface charge model of corrosion pit initiation and of protection by surface alloying. J Electrochem Soc 1999;146(8):2863.
[42] Yasakau KA, Zheludkevich ML, Ferreira MGS. Lanthanide salts as corrosion inhibitors for AA5083. Mechanism and efficiency of corrosion inhibition. J Electrochem Soc 2008;155(5):C169.
[43] Liu X, Wang K, Zhou Y, Zhang X, Tang X, Ren P, et al. In-situ fabrication of Ce-rich CeO2 nanocatalyst for efficient CO oxidation. J Alloys Compd 2019;792:644.
[44] Yin B, Fang L, Tang A-q, Huang Q-l, Hu J, Mao J-h, et al. Novel strategy in increasing stability and corrosion resistance for super-hydrophobic coating on aluminum alloy surfaces. Appl Surf Sci 2011;258(1):580.
[45] Martin Beneke SN. In: ASETSDefense, editor. Chromate free surface pre-treatments for aluminium alloys. AIRBUS; 2016.
[46] Rubio MG. Optimisation of a non-chromium-containing tartaric acid/sulphuric acid anodising bath for aluminium alloys for aerospace industry application (PhD Thesis). Autonomous University of Madrid; 2009.
[47] Savas TP, Earthman JC. Fatigue crack nucleation studies on sulfuric acid anodized 7075-T73 aluminum. J Mater Eng Perform 2014;23(6):2131.

[48] Rateick RG, Griffith RJ, Hall DA, Thompson KA. Relationship of microstructure to fatigue strength loss in anodised aluminium–copper alloys. Mater Sci Technol 2005;21(10):1227.
[49] Sadeler R. Effect of a commercial hard anodizing on the fatigue property of a 2014-T6 aluminium alloy. J Mater Sci 2006;41:5803.
[50] Zhao X, Wei G, Yu Y, Guo Y, Zhang A. An analysis of mechanical properties of anodized aluminum film at high stress. Surf Rev Lett 2015;22.
[51] Lee E, Jeong Y, Kim S. S-N Fatigue behavior of anodized 7050-T7451 produced in different electrolytes. Metall Mater Trans A 2012;vol. 43.
[52] Yoganandan G, Balaraju JN, Manikandanath NT, Ezhilselvi V, Srivastava M, Nagacharan KV, et al. Surface and electrochemical characteristics of novel chromate-free Mn-V oxyanion sealed tartaric–sulfuric acid anodized coating. J Mater Eng Perform 2018;27(11):6175.